PAPER

Check for updates

Substitution (CH₃, Cl, or Br) effects of the imidazolate linker on benzene adsorption kinetics for the zeolitic imidazolate framework (ZIF)-8†

Ryohei Yagi and Takahiro Ueda [ID] *

Herein, the time dependence of benzene adsorption uptake was examined for ZIF-8, Cl-ZIF-8, and Br-ZIF-8 and analysed using an intra-crystalline (Fick's) diffusion model, yielding the diffusion coefficient and saturated adsorption amount of benzene. The saturated adsorption amount of benzene decreased in the order of ZIF-8, Cl-ZIF-8, and Br-ZIF-8. Notably, ZIF-8, with an intermediate pore volume among the three specimens, accommodated the greatest number of molecules (5.5 molecules per micropore). The activation energy, E_a, and the pre-exponential factor, D_0, for benzene diffusion increased in the order of ZIF-8, Cl-ZIF-8, and Br-ZIF-8. These findings suggest that the 2-methylimidazolate moiety forms an effective attraction interaction with benzene molecules. The D_0 values also yielded the activation entropy, $\Delta S^{\ddagger}$, in the transition state when a benzene molecule passed through a six-membered ring aperture. The $\Delta S^{\ddagger}$ values at 303 K were negative, and their absolute values increased in the order of Br-ZIF-8, Cl-ZIF-8, and ZIF-8. Considering the degree of freedom of translation and rotation of the benzene molecule and the vibration and disorder of the linker, we found that the differences in $\Delta S^{\ddagger}$ were caused by the dynamic local structure of the six-membered ring aperture among the ZIF-8 analogues. Furthermore, infrared spectroscopy revealed a low-wavenumber shift of the C–H stretching band in both the imidazolate moiety and adsorbed benzene molecules. A solid-state ^{13}C-nuclear magnetic resonance spectrum presented a downfield shift of ^{13}C resonance peaks in the imidazolate moiety, suggesting that CH/π interactions reasonably explain the intermolecular interaction between the imidazolate moiety (including the methyl group) and π-electrons of benzene.

Introduction

Metal–organic frameworks, including imidazole derivatives as organic ligands, are referred to as zeolitic imidazolate frameworks (ZIFs). These ZIFs have zeolite-like topologies (such as SOD, A-type zeolite (LTA), and RHO zeolitic structures), in which the Zn(II) or Co(II) ions are tetrahedrally coordinated by

Department of Chemistry, Graduate School of Science, Osaka University, Toyonaka, Osaka 560-0043, Japan. E-mail: ueda@chem.sci.osaka-u.ac.jp

† Electronic supplementary information (ESI) available: Figures of TG-DTA diagrams, nitrogen adsorption isotherms, PXRD patterns, SEM images, size distribution of crystallites, comparison of the data optimisation of a surface barrier model and an intra-crystalline (Fick's) diffusion model, typical examples of the model structure and the stable configuration of a benzene molecule adsorbed on a 6-membered ring aperture, Arrhenius plot of the adsorption rate constant, infrared spectra and results of the deconvolution of the ^{13}C-NMR resonance peaks. Tables of BET surface area and pore volume, average particle size, desorption amount of benzene, results of the non-linear least-squared data fitting for Arrhenius plot, Band assignment of IR spectra and ^{13}C chemical shift data. Additional explanation for evaluation of activation entropy of benzene trapped by six-membered ring aperture and ^{13}C–^{14}N and ^{13}C–$^{79/81}$Br residual dipolar splitting. See DOI: https://doi.org/10.1039/d3cp01662e

imidazole derivatives *via* nitrogen atoms.[1,2] ZIFs are attracting attention as zeolite alternatives owing to their versatile skeletal topology, hydrophobic pores, skeletal flexibility, and chemical and thermal stability.[3,4] Among them, ZIF-8, which is composed of Zn²⁺ ions and 2-methylimidazolate anions, is represented by the formula $[Zn(C_4H_5N_2)_2]_n$ and has the same sodalite structure as LTA. The crystal has a cubic lattice belonging to the $I\bar{4}3m$ space group, with a lattice constant of $a = 1.701$ nm (298 K), $Z = 12$ and a unit lattice volume of 4921 nm.[3,5] The crystal also contains micropores with a diameter of 1.16 nm, which are three-dimensionally connected by eight six-membered ring apertures with a diameter of 0.34 nm. These micropores can accommodate various molecules and are expected to be applied in various fields, such as gas storage and separation, removal of harmful substances, catalysis and drug delivery systems.[6–10]

ZIF-8 is thermally stable up to 550 °C. By contrast, it is chemically stable in NaOH aqueous solutions under alkaline conditions; neutral electrolyte solutions such as NaCl and LiCl; and various solvents such as H₂O, MeOH, and benzene. However, acidic solutions decompose and dissolve ZIF-8. For mechanical stability, non-uniform pressures such as during

This journal is © the Owner Societies 2023

Phys. Chem. Chem. Phys., 2023, **25**, 20585–20596 | **20585**

ball milling induce amorphisation.[11] In addition, negative thermal expansion is observed in ZIF-8.[12,13] All of these changes are characterised by the flexibility of the framework caused by the Zn–Im–Zn bond character. This feature also significantly affects the gas adsorption behaviour of ZIF-8. The adsorption amount increases rapidly at a certain pressure for the adsorption of N_2 and Ar.[14,15] The change in orientation of the 2-methylimidazolate linker expands the six-membered ring apertures (swing effect), resulting in pore diameter expansion from 0.34 nm to 0.40 nm.[5,15,16] This phenomenon, called 'gate adsorption', is an adsorption mechanism caused by the flexibility of the framework in ZIF-8.[17–19]

Meanwhile, diffusion coefficients have also been reported for some molecules larger than the expanded six-membered ring aperture.[20] Furthermore, from the viewpoint of the activation energy of the diffusion of gas molecules, the molecular sieving effect on a typical LTA induces a rapid increase in activation energy as the kinetic diameter of the gas molecule approaches the aperture size. By contrast, the activation energy in ZIF-8 increases linearly in proportion to the kinetic diameter.[21] This fact suggests that ZIF-8 regulates the degree of expansion of the six-membered ring aperture by recognising the size of a gas molecule, which is a unique characteristic of adsorption in ZIF-8 that is not observed in activated carbon and typical zeolites. Such characteristic and unique molecular diffusion behaviour also originates from the flexibility of the framework based on the twisting motion of the 2-methylimidazolate linkers around the Zn–Im–Zn axis, which is referred to as the swing effect. Recently, far-infrared spectroscopy and neutron inelastic scattering experiments have suggested that a type of phonon mode (cooperative large-amplitude vibration of an organic linker) excited by the six-membered ring apertures causes the transient expansion of the aperture.[22] In addition, a low-frequency oscillation mode accompanying rotational motion of the linker has been observed by terahertz spectroscopy,[23] suggesting that the swing effect may trigger gate adsorption. Solid-state deuterium nuclear magnetic resonance (NMR) spectrum[24] and the second moment analysis of the wide-line ^{1}H-NMR spectrum[25] also reveal large-amplitude flipping motion of the 2-methylimidazolate linker with a flipping angle of $55°$; that is, the swing effect of the 2-methylimidazolate linkers causes continuous and transient fluctuations in the six-membered ring apertures through the thermal motion of the linkers. This effect plays an important role in molecular diffusion,[26] guest dynamics,[27] and elastic properties[28] of the ZIF-8 crystal lattice; however, the swing effect has not been clearly observed as a structural change in the crystal structure.

In our most recent studies, through temperature-dependent ^{1}H-NMR spin-lattice relaxation time (^{1}H T_1) measurements, we found that the adsorption of bulky molecules resulted in a slowdown in both the rotation of the methyl group and the large-amplitude flipping of the linkers.[25] For example, in the absence of adsorbed bulky molecules, ^{1}H T_1 could not distinguish the rotation of the methyl group and flipping of the 2-methylimidazolate moiety from each other and yielded a frequency of 0.58 THz as each motional mode at room temperature. When a saturated amount of CCl_4 adsorbed onto ZIF-8, ^{1}H T_1 distinguished the rotation of the methyl group and flipping of the linker, and the frequency of each motional mode decreased to 0.24 and 0.06 THz, respectively, at room temperature. Based on our results, we proposed the transient gate mechanism of ZIF-8 for the adsorption of bulky molecules. In this mechanism, the adsorption of bulky molecules triggers the reduction in the frequency of the thermal motion of the linkers, resulting in prolongation of the transient expansion time of the apertures and promotion of molecular adsorption.[25] Thus, by considering the swing effect from the viewpoint of the molecular motion of the linkers, the adsorption behaviour and diffusion mechanism at the molecular level can be elucidated and understood.

However, to control the adsorption process and diffusion behaviour of ZIF-8 based on the swing effect, a systematic and quantitative discussion regarding (1) the local structure of the six-membered ring aperture and (2) the intermolecular interaction between the organic linkers and the adsorbate molecule is essential. In our previous study, the diffusion coefficients and activation energies of molecular diffusion were evaluated for the adsorption process of various bulky molecules onto ZIF-8.[29] The intermolecular interactions between the 2-methylimidazolate linkers and adsorbates were quantitatively examined, revealing that the large-amplitude flip motion of the linkers was necessary to explain those values. Our aim now is to quantitatively evaluate the intermolecular interaction between the adsorbate molecule and organic linker and to elucidate the local structure of the six-membered ring apertures when a bulky molecule is adsorbed in the micropores of ZIF-8 and its analogues. For this purpose, we examined the substituent effect of the functional group on the imidazolate moiety on the adsorption behaviour, as well as molecular diffusion. Thus, we focused on two analogues of ZIF-8, $[Zn(C_3H_2N_2Cl)_2]_n$ (Cl-ZIF-8) and $[Zn(C_3H_2N_2Br)_2]_n$ (Br-ZIF-8), which are composed of a 2-halogeno-substituted imidazolate ligand ($C_3H_2N_2X$; X = Cl, Br). These crystals exhibit isomorphism with ZIF-8. Both Cl-ZIF-8 and Br-ZIF-8 were reported first by Li et al., who investigated the properties of kinetic separation between propane and propene.[30] Thereafter, the behaviour of CO_2 capture/separation has been studied by density functional theory calculations and grand canonical Monte Carlo simulations.[31,32] In addition, molecular sieving properties based on the hydrophobic/hydrophobic nature of the materials have been evaluated by combining molecular simulations and a quantitative structure–property correlation approach.[33] Furthermore, Chaplais et al. recently reported the detailed crystal structures of these materials,[34] both of which have an isomorphic crystal structure with ZIF-8 and two types of disorders in the orientation of the 2-halogeno-substituted imidazolate linker. The substituent effects on the lattice parameters and porosity have been observed as follows: the lattice cell volume increases in the order of functional groups $CH_3 < Cl < Br$. The space in the unit cell accessible by N_2 increases in the order $Cl < CH_3 < Br$, whereas the pore volume (cm^3 g^{-1}) decreases in the order $Br < Cl < CH_3$.

20586 | *Phys. Chem. Chem. Phys.*, 2023, **25**, 20585–20596

This journal is © the Owner Societies 2023

In this study, the adsorption kinetics of Cl-ZIF-8 and Br-ZIF-8 were analysed using benzene as the bulk adsorbate. Through the time dependence of benzene uptake, we examined the effect of the 2-halogeno-substitutent on the adsorption behaviour. Based on the saturated amount of benzene, the intermolecular structure of benzene in the micropores was discussed to provide insights into the intermolecular interactions between the adsorbate molecules and organic linkers. Next, we examined the local structure of the six-membered ring apertures when a benzene molecule passed through the aperture *via* the activation parameters (activation energies and exponential pre-factors) obtained from the temperature dependence of benzene diffusivity. Furthermore, we obtained information on the intermolecular interaction between organic linkers and benzene by infrared absorption spectrum and solid-state ^{13}C-NMR spectrum measurements. To the best of our knowledge, this study is the first to investigate the role of a substituent group in the adsorption kinetics for ZIF-8 analogues. We believe that this study will provide new and additional insights for understanding the adsorption mechanism of bulky molecules into ZIF-8 analogues.

Experimental

Chemicals

Zinc nitrate hexahydrate ($Zn(NO_3)_2 \cdot 6H_2O$, 99.0%), 2-methylimidazole ($C_4H_6N_2$, 98%), 2-chloroimidazole ($C_3H_2N_2Cl$, 96%), ammonium hydroxide, NH_4OH (28 wt%), and ethanol (C_2H_5OH, 99.5%) were purchased from FUJIFILM Wako Pure Chemical Co. 2-Bromoimidazole ($C_3H_2N_2Br$, 97%) was purchased from Fluoro Chem Ltd. All chemicals were used without further purification.

Synthesis

ZIF-8. ZIF-8 was synthesised according to a reported method in the literature.[35] $Zn(NO_3)_2 \cdot 6H_2O$ (0.59 g, 2.0 mmol) was dissolved in 3 mL deionised water by stirring (denoted as solution A), and 2-methylimidazole (0.33 g, 4.0 mmol) was dissolved in 4.3 mL of 28% aqueous ammonia by stirring (denoted as solution B). Solution A was immediately poured into solution B and vigorously stirred, resulting in a white suspension. The suspension was centrifuged at 4000 rpm for 10 min, and the resultant white solid was washed with deionised water for six times. The obtained white precipitate was sealed together with silica gel and then dried at 80 °C for 16 h using an electric dryer. After drying, the amount of the white powder sample was 0.32 g (the yield based on the content of 2-methylimidazole was 68%).

Cl-ZIF-8 and Br-ZIF-8. Cl-ZIF-8 was synthesised according to a method reported in the literature.[34] $Zn(NO_3)_2 \cdot 6H_2O$ (1.31 g, 4.4 mmol) was dissolved in 71 g of ethanol (1536 mmol) in a 150 mL poly(tetrafluoroethylene)-lined stainless-steel autoclave. Then, 2-chloroimidazole (0.90 g, 8.8 mmol) was added to the solution and dissolved completely by stirring for 10 min. The resultant mixture was sealed in a stainless-steel autoclave and heated in a thermostatic electric autoclave at 100 °C for

60 h. After the mixture was cooled to room temperature, a slightly yellowish white precipitate was obtained. The resultant precipitate was centrifuged at 4000 rpm for 10 min, washed using ethanol for five times, and dried using the same procedure as that in the synthesis of ZIF-8. The amount of the resultant ecru powder was 0.77 g (a yield based on the content of 2-chloroimidazole is 66%). The Br-ZIF-8 specimen was synthesised using the same procedure as that of Cl-ZIF-8 but with 2-bromoimidazole instead of 2-chloroimidazole. The amount of the chemicals used was 0.69 g of $Zn(NO_3)_2 \cdot 6H_2O$ (2.3 mmol), 0.68 g of 2-bromoimidazole (4.6 mmol), and 37 g of ethanol (805 mmol). The amount of the obtained ecru powder was 0.74 g (a yield based on the content of 2-bromoimidazole was 90%).

Characterisations

Thermogravimetry/differential thermal analysis. To confirm the pretreatment temperature and presence or absence of solvent in the synthesised specimens (ZIF-8, Cl-ZIF-8, and Br-ZIF-8), thermogravimetry/differential thermal analysis (TG-DTA) measurements were carried out using a TG-DTA2000SA system (Bruker AXS). All thermograms were recorded in the temperature range from room temperature to 400 °C. A 5–10 mg powder sample was mounted on an aluminium pan and heated together with a reference sample of α-Al_2O_3 powder at a heating rate of 5 K min^{-1} under N_2 gas flow (120 cc min^{-1}). The TG and DTA diagrams are shown in Fig. S1 (ESI†).

Nitrogen adsorption isotherm. Nitrogen adsorption isotherms were recorded using a Gemini 2375 apparatus (Shimadzu Corporation) to determine the pore volume and specific surface area of the synthesised samples. The isotherms were recorded in the relative pressure (P/P_0) range of 0.0001–0.98, where P_0 is the saturated vapour pressure of nitrogen at the liquid nitrogen temperature (77 K). The adsorption of N_2 was regarded as reaching equilibrium when the pressure was maintained at a constant value for 10 s. Prior to the measurement, the sample was pretreated by evacuation under a reduced pressure of 2.7 Pa (20 mTorr) at 200 °C for 12 h. The nitrogen adsorption isotherms are depicted in Fig. S2 (ESI†), and the Brunauer–Emmett–Teller (BET) surface areas and pore volumes are listed in Table S1 (see ESI†).

Powder X-ray diffraction. Powder X-ray diffraction (PXRD) patterns were measured using a MiniFlex600 powder X-ray diffractometer (Rigaku Co., Ltd) in the range of 2θ from 3° to 60° with a step of 0.01° at room temperature. Diffraction was conducted using Cu Kα irradiation with a wavelength of 1.5418 Å. The PXRD patterns are presented in Fig. S3 (see ESI†).

Scanning electron microscopy. Scanning electron microscopy (SEM) was performed using a field emission scanning electron microscope SU6600 (Hitachi High-Technologies Co.) to examine the size distribution and morphology of the crystallites. The secondary electron resolution was 1.3 nm. An acceleration voltage of 5.0 kV was used for ZIF-8 and Cl-ZIF-8, whereas 10.0 kV was used for Br-ZIF-8. The SEM images were recorded at a magnification of 5000–45 000×. The SEM images and size distribution of the crystallites are shown in Fig. S4 and S5 (see ESI†).

This journal is © the Owner Societies 2023

Phys. Chem. Chem. Phys., 2023, **25**, 20585–20596 | **20587**

Infrared spectroscopy. Infrared (IR) absorption spectroscopy measurements were carried out using an FT/IR-4600AC spectrometer (JASCO Co.) in the wavenumber range of 400–4000 cm^{-1} at ambient temperature. The wavenumber resolution was 1 cm^{-1}. To avoid amorphisation of ZIF-8 due to pressurisation during the preparation of the KBr pellet sample, the powder sample was sandwiched between two KBr plates and fixed to the sample folder using a magnet. The spectra were recorded in terms of transmittance and converted to absorbance.

Solid-state ^{13}C NMR spectroscopy. The high-resolution solid-state ^{13}C NMR spectra were recorded using an Agilent VNS600 spectrometer equipped with a superconducting magnet (14.7 T). This magnetic field yields a resonance frequency of 600 MHz for ^{1}H nuclei and 150.9 MHz for ^{13}C nuclei. The free induction decay signals of the ^{13}C nuclei were obtained using a single-pulse method under ^{1}H decoupling conditions. The powdered sample was packed in a cylindrical zirconia rotor with a diameter of 3.2 mmø and spun at a speed of 12 kHz for magic-angle sample spinning. Adamantane was used as the external standard for chemical shift, in which the peak of CH$_2$ was ascribed to 38.5 ppm (from tetramethylsilane).

Molecular mechanics. The orientation of benzene molecules near the aperture of the six-membered ring in X-ZIF-8 was estimated using the geometry optimisation function of Avogadro software.[36] The structures of the six-membered ring apertures were extracted from the crystal structures of ZIF-8, Cl-ZIF-8, and Br-ZIF-8. This information can be found in Fig. S7 (see ESI†). Initially, the benzene molecules were randomly oriented in the centre of the bottleneck area above and below the aperture plane. Structural optimisation using molecular mechanics (MM) was performed in the systematic search mode with an energy convergence of ≤10^{-7}. Structural optimisation was conducted only for benzene molecules while the structure of the six-membered ring aperture were maintained fixed in the crystal structure. The top and bottom of the six-membered ring aperture create distinct energy environments for the benzene molecule owing to the different atomic groups that compose the bottleneck. The orientation of the benzene molecule near the aperture of the six-membered ring was determined by computing the average structure from different environments.

Adsorption rate measurements

The samples (ZIF-8, Cl-ZIF-8, and Br-ZIF-8) were packed into an aluminium pan for TG-DTA measurement after pretreatment (evacuation at 200 °C and 2.7 Pa for 12 h). The specimens used were *ca.* 6 mg ZIF-8, *ca.* 8 mg Cl-ZIF-8, and *ca.* 10 mg Br-ZIF-8. The Al pan was placed in a closed container together with 3 mL of benzene (99.5%). Air coexisting in the container affects the adsorption of benzene vapour less because N$_2$ and O$_2$ at ambient temperature are supercritical gases. This container was fixed to a pedestal constructed from heat-insulating Styrofoam and then stored in a thermostatic chamber at 30 °C, 40 °C, and 50 °C, controlled within ±0.5 °C. The sample weight was measured at appropriate time intervals and recorded until a constant value was obtained. This procedure was repeated thrice, and the results were averaged to evaluate the experimental error.

Results and discussion

Time dependence of benzene uptake

Fig. 1(a), (b), and (c) show the time dependence of the adsorption uptake of benzene measured at 303, 313, and 323 K, respectively. The sample weight of each specimen increased rapidly at the initial stage of adsorption and asymptotically approached the saturated value. In the order of ZIF-8, Cl-ZIF-8, and Br-ZIF-8, the saturated adsorption amount of benzene decreased, whereas the increasing rate of benzene uptake to the saturated adsorption amount increased. This trend is consistent with the order of Winstein–Holness A-value[37] (A_{Me} = 1.7, A_{Cl} = 0.43, A_{Br} = 0.38), which is a useful indicator of the substituent effect on reaction selectivity. Therefore, the difference between the adsorption rate and the saturated adsorption amount of benzene among ZIF-8, Cl-ZIF-8, and Br-ZIF-8 is considered to result from the effect of the substituent group on the linker. For a more quantitative discussion on the
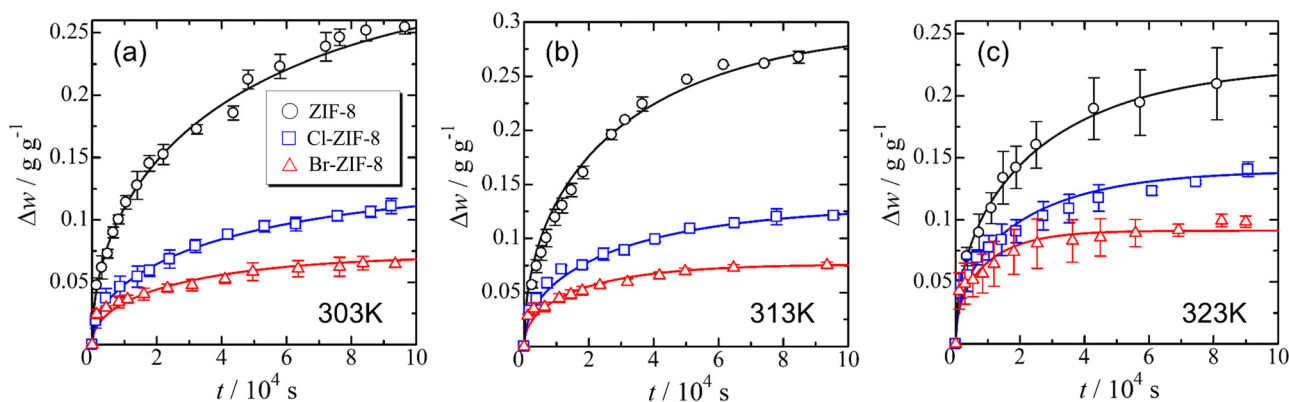

Fig. 1 Time dependence of the adsorption uptake of benzene at 303 (a), 313 (b) and 323 K (c). The solid lines represent the result of the least-square fitting of eqn (2) based on the intra-crystalline (Fick) diffusion model.

20588 | *Phys. Chem. Chem. Phys.*, 2023, **25**, 20585–20596

This journal is © the Owner Societies 2023

substituent effect, the diffusion coefficient and saturated adsorption amount were obtained using the appropriate diffusion model for the adsorption process.

The time dependence of the adsorption uptake is generally denoted by a macroscopic diffusion phenomenon of benzene molecules from the vapour phase to crystallites. Two typical diffusion models exist, namely the surface barrier and intra-crystalline (Fick's) diffusion model.[29,38–41] In the surface barrier model, the diffusion rate is controlled by the penetration resistance on the surface of the crystallites. The time dependence of the uptake, $\Delta w(t)$, obeys the first-order reaction law and is given by the following equation:

$$\Delta w(t) = \Delta w_\infty \left[1 - \exp\left(-\alpha \frac{3}{r_{ave}} t \right) \right] \quad (1)$$

where Δw_∞ is the saturated adsorption amount of the adsorbate, and α is the surface permeability coefficient. The apparent diffusion coefficient, D_s, is given by $\alpha r_{ave}/5$ for a sample with an average particle radius of r_{ave}. In the intra-crystalline (Fick's) diffusion model, the diffusion behaviour is dominated by molecular transformation in the crystallites as the rate-determining process. The time dependence of the uptake follows the Fickian diffusion equation. For spherical particles, $\Delta w(t)$ is given by the following equation:

$$\Delta w(t) = \Delta w_\infty \left[1 - \frac{6}{\pi^2} \sum_{n=1}^{\infty} \frac{1}{n^2} \exp\left(-\frac{n^2 \pi^2 D_f}{r_{ave}^2} t \right) \right] \quad (2)$$

where D_f is the apparent diffusion coefficient. In this study, for each uptake curve, eqn (2) describes the time dependence better than eqn (1) (see Fig. S6 in the ESI†). The diffusion coefficient and saturated adsorption amount of benzene were determined from the optimisation of eqn (2) to the data using the least-squares method. The resultant parameters are listed in Table 1, together with the number of benzene molecules occupying a cage at saturation. The saturated amount of benzene was also confirmed by the weight loss of the samples that reached saturation using TG measurements (see Table S3 in ESI†).

As shown in Table 1, the diffusion coefficient of Cl-ZIF-8 is larger than that of Br-ZIF-8, although the adsorption rate exhibits the opposite trend. This finding possibly reflects the difference in particle size between the specimens (r_{ave} = 585 nm for Cl-ZIF-8 and r_{ave} = 320 nm for Br-ZIF-8) because the average particle size is critically affected by the evaluation of the diffusion coefficient from the adsorption rate. In addition, the diffusion coefficient in the appropriate temperature region is given by the balance between the exponential pre-factor D_0 and the activation energy E_a. Depending on both D_0 and E_a values as described below, Cl-ZIF-8 may also have a larger diffusion coefficient than Br-ZIF-8 in the observed temperature range (303 K $\leq T \leq$ 323 K). In the following sections, based on the saturated adsorption amount of benzene and the diffusion coefficients, we discuss the intermolecular structure of benzene, adsorbent–adsorbate interactions, and the diffusion behaviour of benzene in each specimen.

Saturated adsorption amount of benzene

Fig. 2 shows a plot of the average number (N_{ads}) of benzene and nitrogen molecules occupying a micropore versus micropore volume. The N_{ads} values of benzene used the saturated adsorption amounts at 303 K. The N_{ads} value of the N_2 molecule increases linearly against the pore volume, whereas for the benzene molecule, ZIF-8 with an intermediate pore volume among the three specimens can accommodate the greatest number of molecules in the micropore (5.5 molecules per micropore). The slope of this plot yields the effective density of the adsorbate in the micropores. For nitrogen, the slope is 17.4 molecules nm^{-3}, which agrees well with the bulk density at the triple-point of N_2. This result is as expected because the pore volume is determined from the N_2 adsorption isotherms at 77 K. By contrast, the slope of the line passing through the data point between Br-ZIF-8 and Cl-ZIF-8 is 2.3 molecules nm^{-3}, which corresponds to approximately 36% of the bulk density for liquid benzene. This indicates that the effective volume accessible to benzene molecules is approximately 36% of the pore volume determined from the N_2 adsorption isotherms. Approximating that the micropore shape is a sphere, the reduction in pore volume corresponds to shortening the radius of the sphere by 70.8%. This apparent shrinkage of the micropores is caused by the difference in effective size between the nitrogen and benzene molecules. One of the Lenard–Jones parameters, σ, that is, the distance where the potential energy becomes zero, is 3.70 Å for N_2 and 5.26 Å for liquid benzene.[42]

Table 1 Adsorption rate, diffusion coefficient, and saturated adsorption amount of benzene determined from time dependence of benzene uptake for each specimen

	T/K	$k_{ads.}/10^{-5}$ s^{-1}	r_{ave}/nm	$D_f/10^{-19}$ m^2 s^{-1}	Δw_∞/g g^{-1}	N_{ads}/cage
ZIF-8	303	1.5 ($\pm$0.1)	235 ($\pm$50)	0.84 ($\pm$0.4)	0.29 ($\pm$0.01)	5.5
	313	2.4 ($\pm$0.1)		1.3 ($\pm$0.5)	0.29 ($\pm$0.01)	5.5
	323	2.9 ($\pm$0.3)		1.6 ($\pm$0.7)	0.22 ($\pm$0.02)	4.3
Cl-ZIF-8	303	1.6 ($\pm$0.1)	585 ($\pm$100)	5.6 ($\pm$2)	0.13 ($\pm$0.01)	2.8
	313	2.5 ($\pm$0.1)		8.7 ($\pm$3)	0.13 ($\pm$0.01)	2.8
	323	3.8 ($\pm$0.1)		13.2 ($\pm$5)	0.14 ($\pm$0.01)	3.1
Br-ZIF-8	303	2.6 ($\pm$0.1)	320 ($\pm$50)	2.7 ($\pm$0.9)	0.07 ($\pm$0.01)	2.1
	313	4.2 ($\pm$0.1)		4.4 ($\pm$1.5)	0.08 ($\pm$0.01)	2.3
	323	8.1 ($\pm$0.2)		8.4 ($\pm$2.5)	0.09 ($\pm$0.02)	2.7

The errors estimated in k_{ads}, r_{ave}, D_f, and Δw_∞ are presented in parentheses. The errors in D_f are mainly caused by the errors in the average particle sizes.
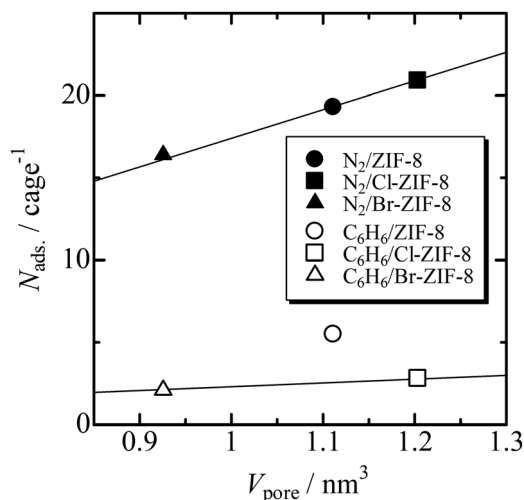
Fig. 2 Average number (N_{ads}) of benzene and nitrogen molecules occupying a micropore plotted against the volume of a micropore (V_{pore}) determined from the N_2 adsorption isotherm. The N_{ads} values of benzene are determined from the saturated adsorption amounts at 303 K. The effective density of adsorbate molecules in the micropore is derived from the slope of each dataset.

The ratio of these values is 0.703, which is consistent with the reduction in the radius of the empty sphere; that is, the slope of the line passing through the data point between Br-ZIF-8 and Cl-ZIF-8 is valid as the effective density of the adsorbed benzene. Thus, the large uptake of benzene by ZIF-8 is an anomaly in comparison with those of Cl-ZIF-8 and Br-ZIF-8, implying a specific attractive interaction between the methyl group and benzene.

In our previous study, we found that for bulky molecules, the stable adsorption sites were located beside the six-membered ring aperture.[25,29] Therefore, we estimated the orientation of a benzene molecule adsorbed on the stable site, as well as the distance between the stable site and the surface of the six-membered ring aperture, using the MM method. MM calculations were performed using the Avogadro software,[36] and the universal force field was used as the molecular force field.[43] Some orientations and distances with similar stable energies within several kilojoules per mole were obtained depending on the initial orientation of benzene.

In addition, Cl-ZIF-8 and Br-ZIF-8 have disordered structures in the linker orientations.[34] In the crystal, each specimen has two different linker orientations with approximately equal populations. Some typical examples of the stable configuration are shown in Fig. S8 in the ESI.† The angle between the aperture surface and the molecular plane of benzene, as well as the distance between the aperture surface and the centre of gravity of the benzene molecule, was evaluated by averaging several orientations and distances for all possible structures of the six-membered ring apertures, as listed in Table 2.

The stable sites occupied by benzene molecules become distant from the six-membered ring aperture surface in the following order: ZIF-8, Cl-ZIF-8, and Br-ZIF-8. In addition, the angle formed by the molecular plane of benzene with respect to

Table 2 Distance and angle between the benzene molecular plane and surface of the six-membered ring aperture using the MM method

	Orientation of linker	$R_{Benzene-ring}$[a]/nm	$\theta_{Benzene-ring}$/°
ZIF-8		0.2893	40.66
Cl-ZIF-8	Orientation 1	0.3133	7.546
	Orientation 2	0.2705	5.581
	Average	0.2919	6.563
Br-ZIF-8	Orientation 1	0.3111	12.57
	Orientation 2	0.2867	4.512
	Average	0.2989	8.512

[a] $R_{Benzene-ring}$ is the distance measured between the centre of molecular plane and the aperture plane.

the aperture surface of the six-membered ring was less than 10° for Cl-ZIF-8 and Br-ZIF-8, suggesting that the benzene molecule is adsorbed at an orientation in which the molecular plane lies along the aperture surface. By contrast, in ZIF-8, the angle between the molecular plane of benzene and the aperture surface is approximately 40°, indicating that the benzene molecule is adsorbed at an orientation slightly erect with respect to the six-membered ring aperture; that is, the pore walls of ZIF-8 can interact with more benzene molecules than Cl-ZIF-8 and Br-ZIF-8. Furthermore, as denoted later, the CH/π interaction between the methyl protons and π electrons of benzene is considered to contribute to the attractive interaction between the benzene molecule and the ZIF-8 pore wall. These interactions should effectively increase the saturated adsorption amount of benzene in ZIF-8. The interaction between the imidazolate linker and the benzene molecule was also investigated by infrared spectroscopy and solid-state ^{13}C-NMR spectroscopy, as described below.

Temperature dependence of the diffusion coefficient

The diffusion coefficient depends on the temperature in all samples. Therefore, the Arrhenius plot of the diffusion coefficient can be used to determine the activation parameters. The Arrhenius equation represents the diffusion coefficient as follows:

$$D_f = D_0 \exp\left(-\frac{E_a}{RT}\right) \quad (3)$$

where D_0 is the pre-exponential factor, and E_a is the activation energy for benzene diffusion. Fig. 3 shows the Arrhenius plot of diffusion coefficient. Each specimen obeys the Arrhenius law, suggesting that the adsorption process of benzene is dominated by the thermally activated process. The slope and intercept of the Arrhenius plot typically provide the activation parameters. However, significant errors in the average particle size result in relatively large errors in D_f. Thus, the activation parameters were evaluated from the Arrhenius plot of the adsorption rate constant, k_{ads} (see Fig. S9 and Table S4 in the ESI†), which included relatively minor errors, as listed in Table 1. The resulting Arrhenius parameters are shown in Table 3.

Both the activation energy and pre-exponential factor increase in the following order: ZIF-8, Cl-ZIF-8, and Br-ZIF-8. The change in activation energy reflects the interaction between
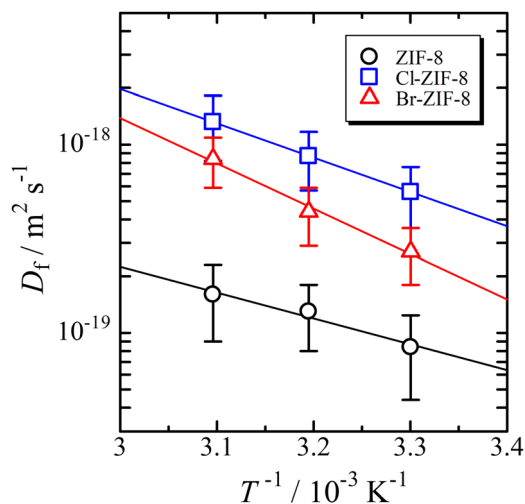
20590 | *Phys. Chem. Chem. Phys.*, 2023, **25**, 20585–20596

This journal is © the Owner Societies 2023

Fig. 3 Arrhenius plot of the diffusion coefficient. The solid lines are the results of the optimisation of eqn (3) to the data using the least-squares method.

Table 3 Activation parameters determined from the temperature dependence of the diffusion coefficient

	E_a/kJ mol^{-1}	D_0/m^2 s^{-1}	$\Delta S^{\ddagger}$/J K^{-1} mol^{-1}
ZIF-8	27 ($\pm$ 2)	$(4 \pm 2) \times 10^{-15}$	-190 ($\pm$ 7)
Cl-ZIF-8	35 ($\pm$ 1)	$(6.5 \pm 2.4) \times 10^{-13}$	-149 ($\pm$ 3)
Br-ZIF-8	46 ($\pm$ 2)	$(2.4 \pm 0.8) \times 10^{-11}$	-138 ($\pm$ 3)

The errors estimated in E_a, D_0, and $\Delta S^{\ddagger}$ are presented in parentheses. The E_a and D_0 values are evaluated from the Arrhenius plot of k_{ads}. The errors in D_f are mainly caused by the errors in the average particle sizes.

benzene and the six-membered ring aperture when a benzene molecule passes through the aperture. The activation energy between Cl-ZIF-8 and Br-ZIF-8 reflects the difference in the van der Waals radius of halogen (r_{Cl} = 175 pm and r_{Br} = 183 pm);[44] that is, the bromine atom induces a larger repulsive interaction with benzene than the chlorine atom, leading to a larger E_a value for Br-ZIF-8. Meanwhile, the methyl group has a van der Waals radius r_{CH_3}= 207 pm, which is estimated using a CH bond distance of 97 pm. This radius is larger than those of chlorine and bromine atoms. Nevertheless, the activation energy of ZIF-8 is smaller than that of Cl-ZIF-8. This finding suggests the occurrence of an attractive interaction that stabilises the transition state of benzene passing through the six-membered ring aperture, which exerts a more effective influence than the repulsive interaction with the methyl group. One of the possibilities for such interactions is the CH/π interaction. This consideration is consistent with the discussion of the saturated adsorption amount mentioned above.

The pre-exponential factor can be discussed based on the transition state theory introduced by Eyring.[45] According to transition state theory, the diffusion coefficient is represented as follows:

$$D = e\lambda^2 \frac{kT}{h} e^{\Delta S^{\ddagger}/R} e^{-E_a/RT} \tag{4}$$

where E_a is the activation energy, $\Delta S^{\ddagger}$ is the activation entropy in the transition state, and λ is the distance at which a benzene molecule jumps beyond a transition state. Here, λ can be regarded as the distance between neighbouring micropores and is given by $\sqrt{3}a_0/2$ as a lattice constant of a_0. By comparing eqn (4) to the Arrhenius equation, the following formula is obtained as a pre-exponential factor, D_0:

$$D_0 = e\lambda^2 \frac{kT}{h} e^{\Delta S^{\ddagger}/R} \tag{5}$$

Using D_0, we can estimate the $\Delta S^{\ddagger}$ value in each sample at 303 K, as listed in Table 3. The $\Delta S^{\ddagger}$ values obtained for all the samples are negative, and their absolute values are comparable to or greater than the entropy change for the vapourisation of benzene. This feature suggests that the system loses a large degree of freedom in the transition state, where the benzene molecule passes through the six-membered ring aperture. Thus, considering the trapping of benzene from the gas phase to the six-membered ring aperture, (1) orientational disorder of the imidazolate linkers, (2) and rotation of the methyl group in ZIF-8, (3) the activation entropy can be discussed in terms of the contribution of each degree of freedom.

During adsorption, benzene molecules lose the degree of freedom of translation, which is accompanied by a significant reduction in entropy. This entropy change is similar to that of condensation from the vapour to liquid phase. The enthalpy of vapourisation at the standard boiling point of benzene (T_b = 353.3 K) is 33.9 kJ mol^{-1},[46] given that the entropy of evaporation of benzene is 96 J K^{-1} mol^{-1}. Thus, the entropy changes of approximately -100 J K^{-1} mol^{-1} in $\Delta S^{\ddagger}$ may be associated with the translation of benzene. Considering the partition function of translation and rotation, we can estimate the entropy change of benzene between the gas phase and transition state at which a benzene molecule is trapped on the six-membered ring aperture. Logically, a benzene molecule loses three degrees of freedom in translation (-160 J K^{-1} mol^{-1}) and in rotation modes (-82.7 J K^{-1} mol^{-1}) by trapping at an aperture. These contributions are expected to result in an entropy reduction of -242.7 J K^{-1} mol^{-1} at 303 K (details of the evaluation are given in ESI†). By contrast, the frequency of the torsional vibration of the linker (flipping motion) is reduced to 1/10 by the interaction of bulky molecules, such as CCl$_4$ and benzene, with the six-membered ring aperture.[24,25] This feature increases the entropy on the six-membered ring aperture by 20 J K^{-1} mol^{-1} for a linker because the lower energy induces an increase in the number of vibrational states occupying the same temperature. Therefore, this contribution increases the entropy to 120 J K^{-1} mol^{-1} in the transition state. These three contributions yield a $\Delta S^{\ddagger}$ of -122.7 J K^{-1} mol^{-1}, corresponding to the experimental value of -138 J K^{-1} mol^{-1} for Br-ZIF-8.

Chaplais et al. reported that the imidazolate linkers in ZIF-8 and Cl-ZIF-8 have two orientations corresponding to gate adsorption when N$_2$ adsorbs into the micropores, whereas the orientation of the linkers in Br-ZIF-8 does not change.[34] Therefore, in both ZIF-8 and Cl-ZIF-8, a linker that is dynamically

This journal is © the Owner Societies 2023

Phys. Chem. Chem. Phys., 2023, **25**, 20585–20596 | **20591**

disordered between two orientations fixes its orientation, thereby reducing entropy. Assuming that two orientations for a linker fix to one orientation, this contribution is expected to result in an entropy reduction of -34.6 J K^{-1} mol^{-1} for a six-membered ring aperture directly interacting with a benzene molecule. For ZIF-8 and Cl-ZIF-8, this contribution is added to the above three contributions, resulting in a $\Delta S^{\ddagger}$ of -157.3 J K^{-1} mol^{-1}. This calculation can explain the difference in the $\Delta S^{\ddagger}$ value between Br-ZIF-8 and Cl-ZIF-8.

Furthermore, in ZIF-8, the rotation of the methyl group also contributes to entropy change. The adsorption of benzene increases the activation energy of methyl rotation (or reorientation) from 1.3 kJ mol^{-1} to 5.1 kJ mol^{-1},[24] implying a pseudo-low-temperature effect; that is, the interaction between the methyl groups and benzene molecules cools the methyl group from the free rotor to the restricted reorientating rotor. Consequently, the entropy of a methyl group for rotation is reduced from 27.2 J K^{-1} mol^{-1} to 9.13 J K^{-1} mol^{-1} ($= R \ln 3$). Therefore, this effect results in an entropy reduction of -108.6 J K^{-1} mol^{-1} for 6Me groups per aperture. This contribution can explain the difference in $\Delta S^{\ddagger}$ between ZIF-8 and Cl-ZIF-8.

Thus, the differences in $\Delta S^{\ddagger}$ among ZIF-8, Br-ZIF-8, and Cl-ZIF-8 are caused by the dynamic local structure of the six-membered ring aperture. The magnitude of $\Delta S^{\ddagger}$ significantly affects the diffusion coefficients in the temperature range from 303 K to 323 K, suggesting a significant interaction between benzene and the six-membered ring aperture.

Insights from spectroscopy

IR spectroscopy. Fig. 4 and 5 present the IR spectra in the CH stretching band regions of ZIFs and benzene, respectively (all wavenumber regions of the infrared spectra are depicted in Fig. S10 in ESI†). The absorption bands were assigned by referring to the literature for ZIF-8[47–49] and bulk benzene,[50,51] whereas those of Cl-ZIF-8 and Br-ZIF-8 were attributed based on the analogy of the peak assignments for ZIF-8. The resultant
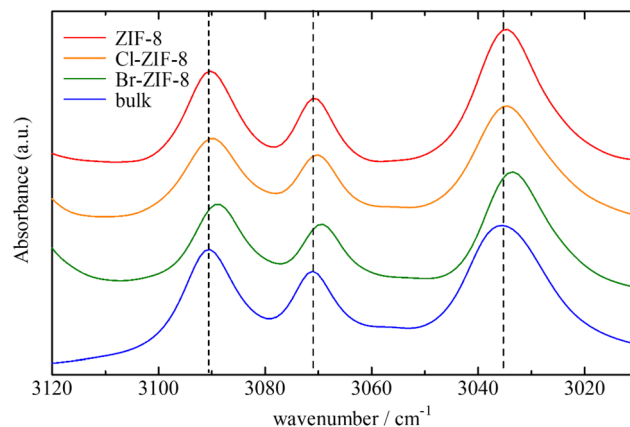

Fig. 5 IR spectra in the CH stretching band regions of benzene in the ZIFs and bulk phase.

assignments are listed in Tables S5–S8 (see ESI†). In Cl-ZIF-8 and Br-ZIF-8, two peaks were observed in the region of the CH stretching band; these peaks can be attributed to the two types of linker orientations resulting from the structural disorder in their crystal structure.

The CH stretching bands of both ZIFs and benzene underwent a remarkable red-shift in the wavenumber range of 1–3 cm^{-1} by benzene adsorption. These shifts demonstrate attractive interactions with protons in the imidazole ring and in benzene. One of the plausible candidates for the attractive interactions acting on the aromatic and aliphatic protons is the C–H/π interaction, which has been observed in a number of organic compounds, metal complexes, and molecular assemblies.[52–58]

In both ZIF-8 and Cl-ZIF-8, the CH stretching band at carbon positions 4 and 5 in the imidazole ring notably shifts to the low-wavenumber side under benzene adsorption conditions. In addition, in ZIF-8, the CH stretching band of the methyl group also shifts to the low-wavenumber side. By contrast, no shift is observed in the corresponding bands for Br-ZIF-8.
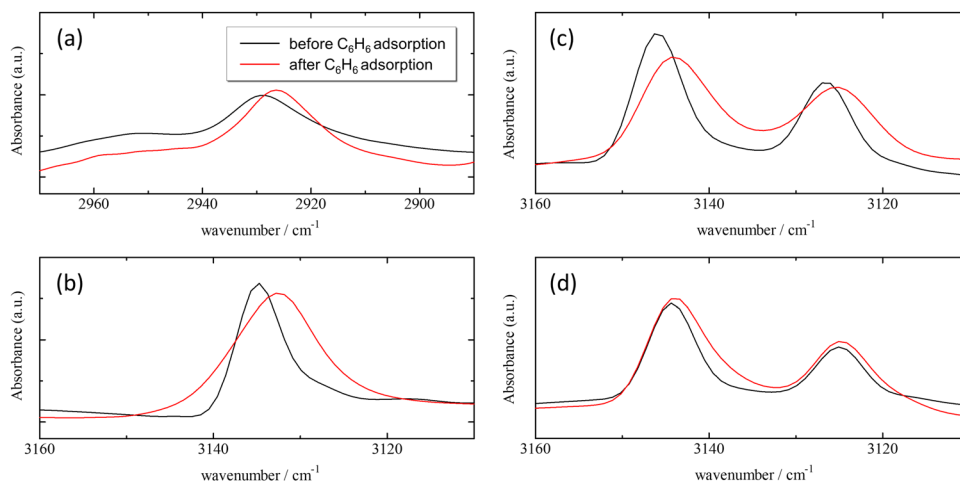

Fig. 4 Infrared spectra in the CH stretching band regions of ZIFs; methyl group (a) and ring proton (b) of ZIF-8, Cl-ZIF-8 (c), and Br-ZIF-8 (d). The double lines of the CH stretching band in Cl-ZIF-8 and Br-ZIF-8 originate from the two different orientations of the linker molecules, which result from structural disorder in their crystal structure.

20592 | *Phys. Chem. Chem. Phys.*, 2023, **25**, 20585–20596

This journal is © the Owner Societies 2023

These results imply that the protons of the imidazole ring in ZIF-8 and Cl-ZIF-8 effectively interact with the π electrons of benzene molecules through CH/π interactions, whereas in Br-ZIF-8, the proton of the imidazole ring does not interact with benzene molecules. Furthermore, the methyl protons also interact with the π electrons of benzene, providing a more effective potential for benzene adsorption in ZIF-8.

Meanwhile, from the viewpoint of benzene molecules, the adsorption of benzene to ZIFs is dominated by the adsorption potential, which is derived by summing up the electrostatic and van der Waals interactions between all atoms in ZIFs and benzene molecules. However, the CH/π interactions between protons in benzene and π electrons of the imidazole ring will affect the molecular orientation of benzene adsorbed into the micropore of each ZIF specimen because intermolecular CH/π interactions are found in aromatic group pairs within 3 Å and in CH_3 and an aromatic ring pair within 2.9 Å.[52–58] Consequently, benzene molecules facilitate orientations that allow the imidazole ring to stand, dominating the local structure of benzene beside the six-membered ring aperture.

Solid-state ^{13}C NMR spectroscopy. Fig. 6 shows the high-resolution solid-state ^{13}C NMR spectra recorded under both magic-angle sample spinning and high-power ^1H decoupling conditions. The upper and lower panels show the spectra
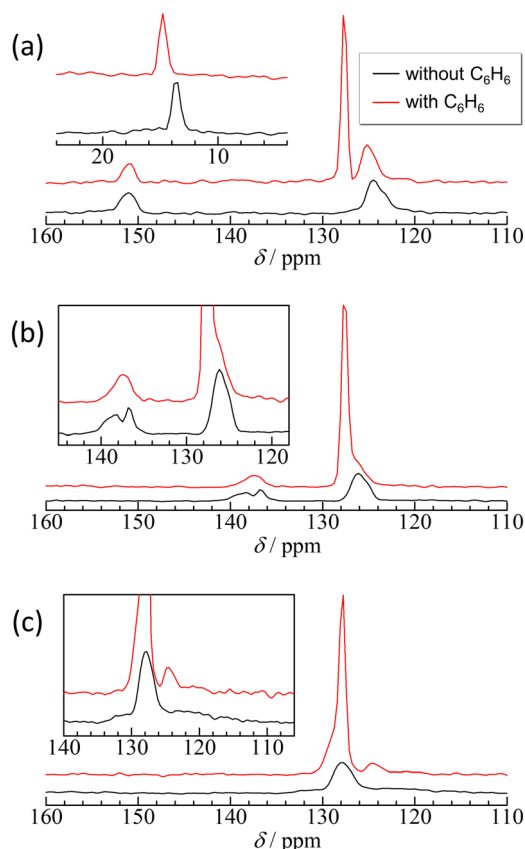

Fig. 6 High-resolution solid-state ^{13}C NMR spectra recorded under both magic-angle sample spinning and high-power ^1H decoupling conditions. The insets depict the extension view around the chemical shift of methyl carbon in ZIF-8 and of imidazole carbons in Cl-ZIF-8 and Br-ZIF-8.

before and after benzene adsorption, respectively. The insets also depict the extension view around the resonance peak of the methyl carbon in ZIF-8 and the imidazole carbons in Cl-ZIF-8 and Br-ZIF-8. According to previous studies,[5,34] the chemical shift range of the framework can be assigned as follows: 13–15 ppm for methyl carbon, 123–126 ppm for aromatic C–H carbons, and 150–152 ppm for the quaternary carbon in ZIF-8; 125–127 ppm for aromatic C–H carbons and 136–139 ppm for the quaternary carbon in Cl-ZIF-8; and 126–129 ppm for aromatic C–H carbons and 120–140 ppm for the quaternary carbon in Br-ZIF-8. The results of the deconvolution of the spectra and the parameters determined are shown in Fig. S11 and Tables S9–S11 (see ESI†).

In ZIF-8, the resonance peak of the imidazole ring is asymmetric, as expected, to determine whether the ^{13}C–^{14}N residual dipolar splitting[59] or the existence of different environments for aromatic C–H carbons and the quaternary carbon. However, the ^{13}C–^{14}N residual dipolar splitting in ZIF-8 is estimated to be <0.2 ppm (see ESI†), which is too small to explain the full width at half maximum of the observed peaks. Therefore, the asymmetric peak implies different environments on the aromatic C–H carbons, probably caused by the different orientations of the linkers. After adsorption of benzene, the resonance peak of benzene shows an upfield shift of 1 ppm in comparison with bulk benzene, whereas the resonance peaks of the frameworks show a downfield shift of approximately 1 ppm, except for the quaternary carbon. These shifts are an evidence of the intermolecular interactions between benzene and the 2-methylimidazole moiety being able to consider the following two types of interactions: The upfield shift (decrease in the chemical shift value) of the aromatic carbons of benzene suggests π–π interactions between benzene and the 2-methylimidazole ring.[60] By contrast, the downfield shift of methyl and aromatic C–H carbons implies CH/π interactions of these protons with the π electrons of benzene.[61,62]

In Cl-ZIF-8 and Br-ZIF-8, the resonance peaks of the aromatic CH carbons are also asymmetric similar to those in ZIF-8 but with smaller splitting, implying the existence of different orientations of the linker. Notably, the resonance of the quaternary carbon of Cl-ZIF-8 was split into two peaks, suggesting that the 2-chloroimidazole linker was disordered into two orientations. After the adsorption of benzene, the resonance peak of the quaternary carbon in Cl-ZIF-8 merges to one peak, indicating that benzene adsorption eliminates the disorder of the linker orientation. By contrast, the resonance of the quaternary carbon of Br-ZIF-8 broadened from 120 ppm to 140 ppm. This broadening may be caused by the dynamic disorder of the linker orientation[34] and/or ^{13}C–$^{79/81}Br$ residual dipolar splitting.[63–65] The ^{13}C–$^{79/81}Br$ residual dipolar splitting in Br-ZIF-8 is estimated to be 15 ppm for ^{81}Br and 19 ppm for ^{79}Br (see ESI†), which is consistent with the observed linewidth for the quaternary carbon of Br-ZIF-8. However, the adsorption of benzene notably made the broadened resonance peak in Br-ZIF-8 narrow and clear, suggesting that the adsorption of benzene slows down the motion of the dynamically disordered linkers. Both cases make it possible to reduce the entropy of the

This journal is © the Owner Societies 2023

Phys. Chem. Chem. Phys., 2023, **25**, 20585–20596 | **20593**

linker orientation, supporting the discussion regarding the activation entropy. The adsorption of benzene affected the local structure of the 2-chloroimidazole and 2-bromoimidazole linkers. After the adsorption of benzene onto Cl-ZIF-8, as well as onto Br-ZIF-8, the resonance peak of benzene also made an upfield shift of 1 ppm in comparison with bulk benzene, suggesting π–π interactions[60] between benzene and 2-chlorolimidazole and/or 2-bromoimidazole rings.

Conclusions

The time dependence of the benzene adsorption uptake of ZIF-8, Cl-ZIF-8, and Br-ZIF-8 was analysed at 303, 313, and 323 K, and the adsorption was well reproduced by an intra-crystalline (Fick's) diffusion model. The diffusion coefficient and saturated adsorption amount of benzene were determined by optimising the model to experimental data.

The saturated adsorption amount of benzene decreased in the order of ZIF-8, Cl-ZIF-8, and Br-ZIF-8. Notably, ZIF-8, which possesses an intermediate pore volume among the three specimens, can accommodate the greatest number of molecules in the micropore (5.5 molecules per micropore). This saturated amount of benzene was much greater than that predicted from the effective density of the adsorbed benzene. MM calculations revealed the closest distance between benzene and the six-membered ring aperture surface and the large tilting angle of the benzene molecule with respect to the aperture surface in ZIF-8. These findings suggest that the 2-methylimidazolate moiety forms an effective attraction interaction with benzene molecules. In this context, the CH/π interaction between the methyl proton and the π electrons of benzene is considered to contribute to the attractive interaction between the benzene molecule and ZIF-8 pore wall.

Both the activation energy and pre-exponential factor increased in the order ZIF-8, Cl-ZIF-8, and Br-ZIF-8. ZIF-8 exhibited the smallest E_a value, despite the expected effective steric hindrance caused by having the largest methyl group among the three specimens. This result suggests the occurrence of an attractive interaction that stabilises the transition state of benzene passing through the six-membered ring aperture, which is consistent with the discussion of the saturated adsorption amount. Furthermore, the pre-exponential factor, D_0, gives the activation entropy, $\Delta S^{\ddagger}$, in the transition state when a benzene molecule passes through a six-membered ring aperture. The $\Delta S^{\ddagger}$ values at 303 K were negative, and their absolute values increased in the order of Br-ZIF-8, Cl-ZIF-8, and ZIF-8. Considering the degree of freedom of translation and rotation of the benzene molecule, as well as the vibration and disorder of the linker, we found that the differences in $\Delta S^{\ddagger}$ were caused by the dynamic local structure of the six-membered ring aperture among the ZIF-8 analogues. The magnitude of $\Delta S^{\ddagger}$ significantly affects the diffusion coefficients in the temperature range from 303 K to 323 K, suggesting a significant interaction between benzene and the six-membered ring aperture.

Infrared spectroscopy revealed that the aromatic C–H in ZIF-8 and Cl-ZIF-8 interacted with the π-electrons in benzene through CH/π interactions, whereas in Br-ZIF-8, the interaction acting on the aromatic C–H might be considerably small. This feature of Br-ZIF-8 is considered to originate from the large steric hindrance around the aromatic C–H because of the larger atomic radius of the bromine atom compared with other functional groups. By contrast, the low-wavenumber shift of the C–H stretching band in benzene suggests that the benzene molecules interact attractively with the π-electrons in the linkers through CH/π interactions. The CH/π interactions between methyl protons and the π-electrons of benzene and between aromatic C–H protons in the frameworks and the π-electrons of benzene were also confirmed by the downfield shift of the ^{13}C resonance peaks for the corresponding carbons. Meanwhile, the π–π interactions between benzene and the 2-methylimidazole ring and between benzene molecules were confirmed by the upfield shift (decrease in the chemical shift value) of the ^{13}C resonance peaks of benzene carbons. Thus, these spectroscopic features revealed that the intermolecular interactions between the linkers and benzene increased in the order of Br-ZIF-8 $\ll$ Cl-ZIF-8 < ZIF-8. This difference in intermolecular interactions is expected to dominate the saturated amount of benzene adsorption.

In summary, this study reveals that the CH/π interaction between the 2-substituted imidazole ligand of X-ZIF-8 and adsorbate molecule provides an energetic advantage when the benzene molecule passes through the six-membered ring aperture and accelerates adsorption. In particular, methyl groups were more effective than halogen groups in the CH/π interaction and also played an important role in the energetic stabilisation of benzene molecules in the pore. This finding suggests that the adsorption of molecules with π-electron systems on ZIF-8 is more favourable than that with non-π-electron compounds. In the future, to further clarify this point, we intend to examine the dependence of the number of π-electrons in the adsorbate on the adsorption behaviour into ZIF-8 by studying the adsorption rate of six-membered ring alicyclic hydrocarbons similar to benzene molecules.

Author contributions

Ryohei Yagi: conceptualisation, methodology, validation, formal analysis, investigation, data curation, writing – original draft, and visualisation. Takahiro Ueda: conceptualisation, methodology, validation, resources, software, formal analysis, visualisation, writing – review & editing, supervision, funding acquisition, project administration.

Conflicts of interest

There are no conflicts to declare.

Acknowledgements

20594 | *Phys. Chem. Chem. Phys.*, 2023, **25**, 20585–20596

This journal is © the Owner Societies 2023

Notes and references

1 A. Phan, C. J. Doonan, F. J. Uribe-Romo, C. B. Knobler, M. O'Keeffe and O. Y. Yaghi, *Acc. Chem. Res.*, 2010, **43**(1), 58.

2 R. Banerjee, A. Phan, B. Wang, C. Knobler, H. Furukawa, M. O'Keeffe and O. M. Yaghi, *Science*, 2008, **319**, 939.

3 L. B. D. Bourg, A. U. Ortiz, A. Boutin and F.-X. Coudert, *APL Mater.*, 2014, **2**, 124110.

4 K. S. Park, Z. Ni, A. P. Cote, J. Y. Choi, R. Huang, F. J. Uribe-Romo, H. K. Chae, M. O'Keeffe and O. M. Yaghi, *Proc. Natl. Acad. Sci. U. S. A.*, 2006, **103**, 10186.

5 W. Morris, C. J. Stevens, R. E. Taylor, C. Dybowski, O. M. Yaghi and M. A. Garcia-Garibay, *J. Phys. Chem. C*, 2012, **116**, 13307.

6 P. Cheng and Y. H. Hu, *J. Phys. Chem. C*, 2014, **118**, 21866.

7 K. Eum, K. C. Jayachandrababu, F. Rashidi, K. Zhang, J. Leisen, S. Graham, R. P. Lively, R. R. Chance, D. S. Sholl, C. W. Jones and S. Nair, *J. Am. Chem. Soc.*, 2015, **137**, 4191.

8 S. El-Hankari, J. Aguilera-Sigalat and D. Bradshaw, *J. Mater. Chem. A*, 2016, **4**, 13509.

9 D. M. Polyukhov, A. S. Poryvaev, A. S. Sukhikh, S. A. Gromilov and M. V. Fedin, *ACS Appl. Mater. Interfaces*, 2021, **13**, 40830.

10 H. Zhao, H. Ye, J. Zhou, G. Tang, Z. Hou and H. Bai, *ACS Appl. Mater. Interfaces*, 2020, **12**, 49431.

11 L. Zhang and Y. H. Hu, *J. Phys. Chem. C*, 2011, **115**, 7967.

12 V. Eroshenko, Y. Grosu, N. Tsyrin, V. Stoudenets, J.-M. Nedelec and J.-P. E. Grolier, *J. Phys. Chem. C*, 2015, **119**, 10266.

13 A. F. Sapnik, H. S. Geddes, E. M. Reynolds, H. H.-M. Yeung and A. L. Goodwin, *Chem. Commun.*, 2018, **54**, 9651.

14 L. Zhang, Z. Hu and J. Jiang, *J. Am. Chem. Soc.*, 2013, **135**, 3722.

15 H. Tanaka, S. Ohsaki, S. Hiraide, D. Yamamoto, S. Watanabe and M. T. Miyahara, *J. Phys. Chem. C*, 2014, **118**, 8445.

16 C. O. Ania, E. García-Perez, M. Haro, J. J. Gutierrez-Sevillano, T. Valdes-Solis, J. B. Parra and S. Calero, *J. Phys. Chem. Lett.*, 2012, **3**, 1159.

17 D. Fairen-Jimenez, S. A. Moggach, M. T. Wharmby, P. A. Wright, S. Parsons and T. Düren, *J. Am. Chem. Soc.*, 2011, **133**, 8900.

18 T. Tian, M. T. Wharmby, J. B. Parra, C. O. Ania and D. Fairen-Jimenez, *Dalton Trans.*, 2016, **45**, 6893.

19 F.-X. Coudert, *ChemPhysChem*, 2017, **18**, 2732.

20 C. Zhang, R. P. Lively, K. Zhang, J. R. Johnson, O. Karvan and W. J. Koros, *J. Phys. Chem. Lett.*, 2012, **3**, 2130.

21 K. Zhang, R. Lively, C. Zhang, R. Chance, W. Koros, D. Sholl and S. Nair, *J. Phys. Chem. Lett.*, 2013, **4**, 3618.

22 M. R. Ryder, B. Civalleri, T. D. Bennett, S. Henke, S. Rudić, G. Cinque, F. Fernandez-Alonso and J.-C. Tan, *Phys. Rev. Lett.*, 2014, **113**, 215502.

23 N. Y. Tan, M. T. Ruggiero, C. Orellana-Tavra, T. Tian, A. D. Bond, T. M. Korter, D. Fairen-Jimenez and J. A. Zeitler, *Chem. Commun.*, 2015, **51**, 16037.

24 D. I. Kolokolov, A. G. Stepanov and H. Jobic, *J. Phys. Chem. C*, 2015, **119**, 27512.

25 T. Ueda, M. Nakai and T. Yamatani, *Adsorption*, 2017, **23**, 887.

26 A. Awadallah-F, F. Hillman, S. A. Al-Muhtaseb and H.-K. Jeong, *J. Mater. Sci.*, 2019, **54**, 5513.

27 A. E. Khudozhitkov, H. Zhao, A. Ghoufi, S. S. Arzumanov, D. I. Kolokolov, G. Maurin and A. G. Stepanov, *ACS Appl. Mater. Interfaces*, 2021, **13**, 33685.

28 D. Radhakrishnan and C. Narayana, *J. Chem. Phys.*, 2015, **143**, 234703.

29 T. Ueda, T. Yamatani and M. Okumura, *J. Phys. Chem. C*, 2019, **123**, 27542.

30 K. Li, D. H. Olson, J. Seidel, T. J. Emge, H. Gong, H. Zeng and J. Li, *J. Am. Chem. Soc.*, 2009, **131**, 10368.

31 H. Amrouche, S. Aguado, J. Perez-Pellitero, C. Chizallet, F. Siperstein, D. Farrusseng, N. Bats and C. Nieto-Draghi, *J. Phys. Chem. C*, 2011, **115**, 16425.

32 J. Hu, Y. Liu, J. Liu and C. Gu, *Fuel*, 2017, **200**, 244.

33 H. Amrouche, B. Creton, F. Siperstein and C. Nieto-Draghi, *RSC Adv.*, 2012, **2**, 6028.

34 G. Chaplais, G. Fraux, J.-L. Paillaud, C. Marichal, H. Nouali, A. H. Fuchs, F.-X. Coudert and J. Patarin, *J. Phys. Chem. C*, 2018, **122**, 26945.

35 B. Chen, F. Bai, Y. Zhu and Y. Xia, *Microporous Mesoporous Mater.*, 2014, **193**, 7.

36 M. D. Hanwell, D. E. Curtis, D. C. Lonie, T. Vandermeersch, E. Zurek and G. R. Hutchison, *J. Cheminformatics*, 2012, **4**, 17.

37 B. S. Winsten and N. J. Holness, *J. Am. Chem. Soc.*, 1955, **77**, 5562.

38 S. Tanaka, K. Fujita, Y. Miyake, M. Miyamoto, Y. Hasegawa, T. Makino, S. Van der Perre, J. C. Saint Remi, T. Van Assche, G. V. M. Baron and J. F. M. Denayer, *J. Phys. Chem. C*, 2015, **119**, 28430.

39 J. Kärger, D. M. Ruthven and D. N. Theodorou, *Diffusion in nanoporous materials*, Wiley-VCH, Weinheim, Germany, 2012.

40 L. Zhang, C. Chmelik, A. N. C. van Laak, J. Kärger, P. E. de Jongh and K. P. de Jong, *Chem. Commun.*, 2009, 6424.

41 S. Sircar and J. R. Hufton, *Adsorption*, 2000, **6**, 137.

42 E. Wilhelm and R. Battino, *J. Chem. Phys.*, 1971, **55**, 4012.

43 A. K. Rappé, C. J. Casewit, K. S. Colwell, W. A. Goddard III and W. M. Skiff, *J. Am. Chem. Soc.*, 1992, **114**, 10024.

44 M. Mantina, A. C. Chamberlin, R. Valero, C. J. Cramer and D. G. Truhlar, *J. Phys. Chem. A*, 2009, **113**, 5806.

45 S. Glasstone, K. J. Laidler and H. Eyring, *The Theory of Rate Processes: The Kinetics of Chemical Reactions, Viscosity,*

This journal is © the Owner Societies 2023

Phys. Chem. Chem. Phys., 2023, **25**, 20585–20596 | **20595**

Diffusion and Electrochemical Phenomena, McGraw-Hill, New York, USA, 1941.

46 M. V. Roux, M. Temprado, J. S. Chickos and Y. Nagano, *J. Phys. Chem. Ref. Data*, 2008, **37**(4), 1855.

47 Y. Hu, H. Kazemian, S. Rohani, Y. Huang and Y. Song, *Chem. Commun.*, 2011, **47**, 12694.

48 B. Xu, D. Xie, Y. Mei, Z. Kang, R. Wang and D. Sun, *Phys. Chem. Chem. Phys.*, 2017, **19**, 27178.

49 C. Wu, D. Xie, Y. Mei, Z. Xiu, K. M. Poduska, D. Li, B. Xu and D. Sun, *Phys. Chem. Chem. Phys.*, 2019, **21**, 17571.

50 S. Wang, *Sci. Rep.*, 2020, **10**, 17875.

51 M. A. Palafox, *Int. J. Quantum Chem.*, 2000, **77**, 661.

52 M. Nishio, *CrystEngComm*, 2004, **6**, 130.

53 S. Tsuzuki, *Annu. Rep. Prog. Chem., Sect. C: Phys. Chem.*, 2012, **108**, 69.

54 S. Tsuzuki, K. Honda, T. Uchimaru, M. Mikami and K. Tanabe, *J. Am. Chem. Soc.*, 2000, **122**, 3746.

55 R. M. Kumar, M. Elango, R. Parthasarathi, D. Vijay and V. Subramanian, *J. Chem. Sci.*, 2012, **124**, 193.

56 M. Li, G. Qing, Y. Xiong, Y. Lai and T. Sun, *Sci. Rep.*, 2015, **5**, 15742.

57 G. Platzer, M. Mayer, A. Beier, S. Brüschweiler, J. E. Fuchs, H. Engelhardt, L. Geist, G. Bader, J. Schörghuber, R. Lichtenecker, B. Wolkerstorfer, D. Kessler, D. B. McConnell and R. Konrat, *Angew. Chem., Int. Ed.*, 2020, **59**, 14861.

58 S. Morita, A. Fujii, N. Mikami and S. Tsuzuki, *J. Phys. Chem. A*, 2006, **110**, 10583.

59 K. Eichele, M. D. Lumsden and R. E. Wasylishen, *J. Phys. Chem.*, 1993, **97**, 8909.

60 Y. Zhang, B. Ji, A. Tian and W. Wang, *J. Chem. Phys.*, 2012, **136**, 141101.

61 S. Scheiner, *Chem. Phys. Lett.*, 2019, **714**, 61.

62 G. Li, L. Huang, X. Yi, Y.-K. Peng, S. C. E. Tsang and A. Zheng, *Chem. Commun.*, 2018, **54**, 13435.

63 R. K. Harris and A. C. Olivieri, *Prog. Nucl. Magn. Reson. Spectrosc.*, 1992, **24**, 435.

64 A. C. Olivieri, L. Frydman and L. E. Diaz, *J. Magn. Reson.*, 1987, **75**, 50.

65 A. C. Olivieri, *J. Magn. Reson.*, 1989, **81**, 201.